5. Carbon Nanotubes: Excitons, Localized and Delocalized Carriers

In this chapter, the mid-infrared response of an optically excited carbon-nanotube film is investigated. In contrast to graphite, the data lack a free-carrier response which clearly indicates that strongly bound excitons are the main product of optical excitation in the tubes with energy gaps in the eV range. We find a spectral feature of enhanced transmission which originates from blocked optical transitions in tubes having a small or vanishing energy gap. A featureless background of increased absorption shows a large optical anisotropy and provides direct evidence for the localization of charge carriers on a length scale of ~ 100 nm.

5.1. Motivation

Single-wall carbon nanotubes (NTs) are hollow cylinders made of carbon atoms. Since their discovery in 1991, they have attracted an enormous attention in fundamental and applied research due to their unique properties [Avo04]:

- NTs have a tensile strength many times that of carbon steel, are thermally stable at temperatures of more than $1000\,°C$ in air, and have a thermal conductivity comparable to that of diamond. As a strongly bonded covalent material, they typically show only few defects.

- They are close to a true 1-dimensional system since their diameters are typically only 1 to 3 nm but they can be millimeters long. Thus, they constitute a playground for probing the properties of 1-dimensional solids.

- Depending on their geometry, NTs can be semiconducting with an electronic energy gap of $\sim 1\,eV$ or nearly metallic. For example, the semiconducting tubes can be employed to build a NT-based field-effect transistor as shown in Fig. 5.1. Soon the gate size of such devices is expected to be smaller than that of current silicon-based transistors. Moreover, NTs feature a high threshold for electrical breakdown.
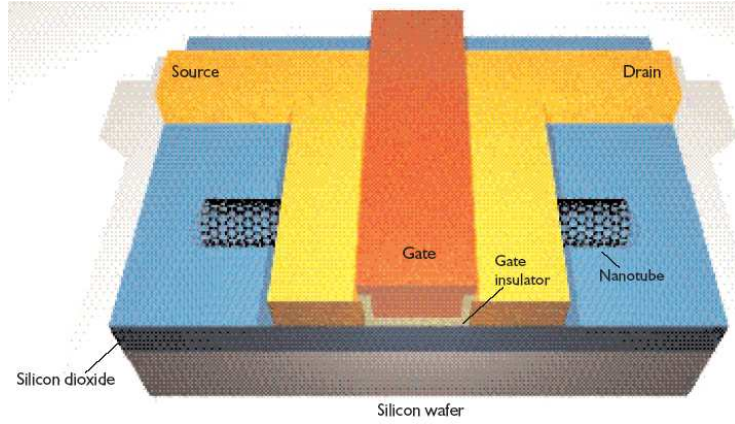
Figure 5.1.: Illustration of NT field-effect transistor, taken from Ref. [Avo04]. The gate voltage is applied between the metallic gate and the conducting silicon substrate. It can switch the conductance between the source and drain electrodes on and off.

In order to realize the great potential of NTs in future nanoelectronics, a comprehensive knowledge of the charge-carrier dynamics in NTs is essential. As mentioned in the introduction to this work, time-resolved THz spectroscopy is a promising approach to this issue.

5.2. General Properties

Figure 5.2 illustrates that NTs can be understood as a rolled-up graphene sheet having lattice basis vectors $\boldsymbol{b}_1$ and $\boldsymbol{b}_2$. The 2 integers n_1 and n_2 characterize the wrapping or chiral direction $n_1\boldsymbol{b}_1 + n_2\boldsymbol{b}_2$ and therefore completely determine the resulting NT as well, for example its diameter $d_{\mathrm{NT}} = |n_1\boldsymbol{b}_1+n_2\boldsymbol{b}_2|/\pi$ [Sai98]. There is still a discrete translational symmetry along the tube axis but the size of the 1-dimensional unit cell depends on (n_1, n_2) and can be considerably larger than the diameter of the hexagonal unit cell of graphene. Consequently, the Brioullin zone (BZ) is also 1-dimensional, and its wavevectors k refer to the direction parallel to the tube axis.

There are several methods to produce NTs. The NTs investigated in this work have been produced by the high-pressure carbon monoxide (HiPCO) method [O'C02] which employs gaseous $Fe(CO)_5$ and CO at $\approx 1000\,°C$ under high pressure. In this reaction, $Fe(CO)_5$ dissociates, and the resulting Fe clusters initiate the growth of NTs where the C atoms derive from the disproportionation of CO. Finally, the HiPCO material is purified to remove catalyst particles.

5.3. Electronic Structure

The NTs investigated in this work have a length of a few $100\,\mathrm{nm}$. Their much smaller diameter of $d_{\mathrm{NT}} \approx 1\,\mathrm{nm}$ leads to remarkable quantum-size effects in the electronic structure.
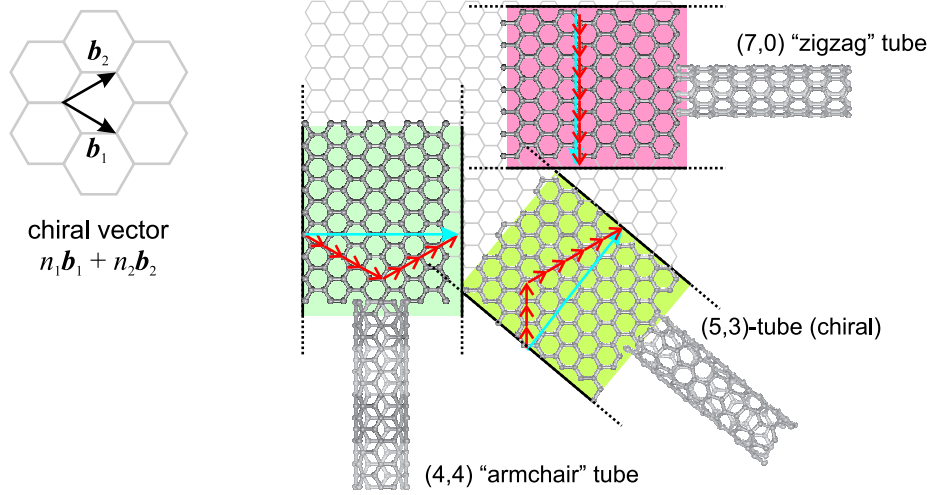
Figure 5.2.: Structure of carbon nanotubes. They can be thought of as rolled-up sheets of graphene where the chiral vector $n_1 \boldsymbol{b}_1 + n_2 \boldsymbol{b}_2$, with n_1 and n_2 being integers, entirely determines the wrapping direction. Depending on (n_1, n_2) the resulting tube is semiconducting or metallic. This figure was taken from Ref. [Hag05a].
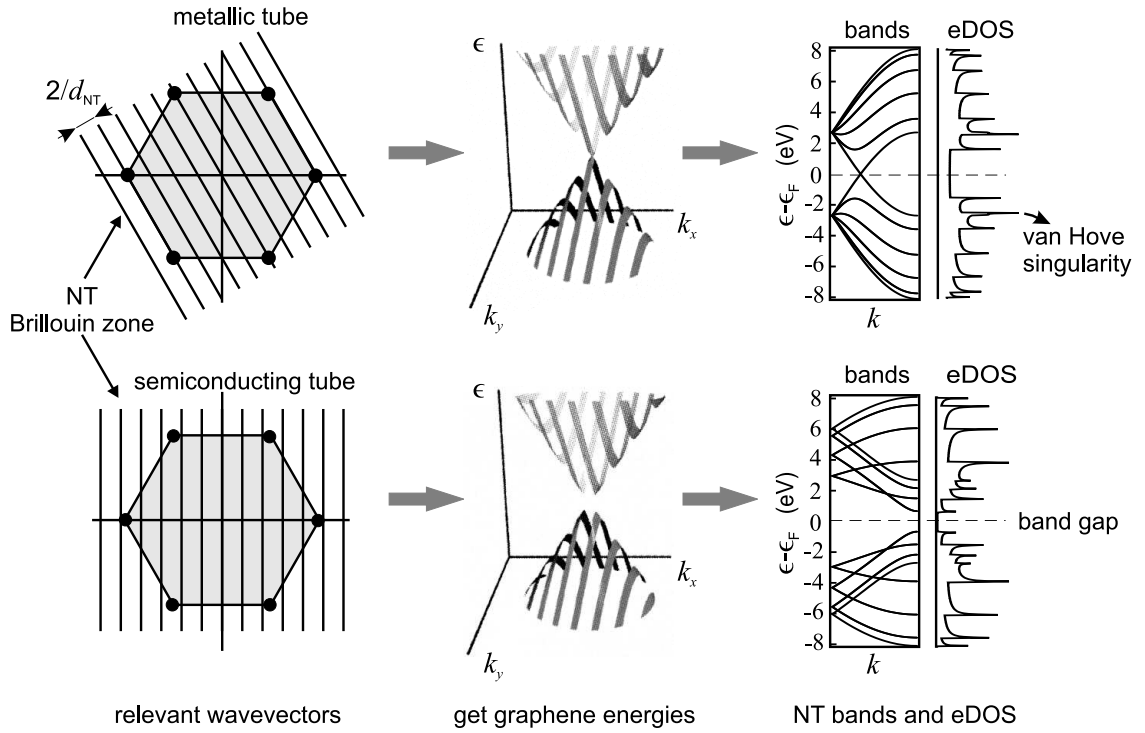

Figure 5.3.: Electronic band structure of NTs derived from that of a graphene sheet. The NT geometry restricts the allowed wavevectors to a series of lines in the (k_x, k_y) space of graphene. Each line leads to a 1-dimensional subband in the k space of the NT where k is the wavevector along the NT axis. If at least 1 of these lines crosses the K or K' point, a metallic NTs without an energy gap is obtained; otherwise, the NT is semiconducting. The resulting eDOS exhibits van Hove singularities at energies where the bands have vanishing slope. This figure was taken from Ref. [Hag05a].

5.3.1. Single-Particle Picture

In a single-electron approach, one can employ tight-binding schemes as done in Section 4.3.1 for graphite to determine the electronic band structure of a NT. The simplest approach relies on the graphene bands where the NT geometry allows only for a subset of the graphene wavevectors $\boldsymbol{k}$ [Sai98]:

- The wavevectors k *parallel* to the tube axis are given by the 1-dimensional BZ of the NT under consideration.

- The wrapping of the graphene sheet is taken into account by periodic boundary conditions for the electron wavefunctions along the wrapping direction $n_1\boldsymbol{b}_1 + n_2\boldsymbol{b}_2$ which allows only for certain graphene wavevectors *perpendicular* to the tube axis.

This so-called zone folding is demonstrated in Fig. 5.3 for 2 different NTs and shows how the geometrical structure can make a NT semiconducting or metallic. Within this framework, it generally can be shown that

NTs with $n_1 - n_2 \notin 3\mathbb{Z}$ are "*large-gap* NTs"

since they are semiconducting with an energy gap of about $1\,\text{eV}$ for tube diameters of $\approx 1\,\text{nm}$. The remaining "NTs are metallic. Consequently, 2/3 of all NT types (n_1, n_2) are large-gap NTs. The electronic density of states (eDOS) in Fig. 5.3 features so-called van Hove singularities which arise from the vanishing slope of 1-dimensional energy bands [Sai98].

The graphene-based model does *not* take into account the curvature of the graphene sheet which modifies the overlap of adjacent p_z orbitals. More sophisticated tight-binding calculations [Din02] show that this curvature introduces additional small band gaps in all metallic NTs apart from the (n, n) "armchair" tubes. These

"*small-gap* NTs" with $n_1 - n_2 \in 3\mathbb{Z}$ and $n_1 \neq n_2$

exhibit band gaps of $\sim 20\,\text{meV}$ for tube diameters of $\approx 1\,\text{nm}$ as found by scanning tunneling spectroscopy [Ouy01].

Strong curvature can also induce an appreciable hybridization of the σ and π bonds between the carbon atoms. Taking this effect into account makes the originally large-gap $(5, 0)$ NT metallic [Spa04]. In addition, environmental perturbations, for example by other NTs in NT ropes, a surrounding solution, or a substrate, can further modify the electronic structure and even open energy gaps [Del98].

5.3.2. Many-Body Effects

Compared to 3-dimensional solids or quasi-2-dimensional solids like graphite, the e-e interaction is expected to be much stronger in the quasi-1-dimensional NTs: In a somewhat

naive picture, the electrons simply cannot "circumvent" each other as they can in higher-dimensional solids.

The picture of independent electrons breaks down at least in the large-gap NTs since there the Coulomb interaction is only weakly screened compared to the small-gap and metallic NTs. As a consequence, electrons and holes form strongly bound excitons with binding energies of up to 1 eV [Spa04]. This is in contrast to 3-dimensional semiconductors like GaAs where exciton binding energies of less than 10 meV are found [Mad78]. The energy spectrum of an exciton is similar to that of a hydrogen atom with discrete energy levels below and a continuum of levels above the binding energy.

The existence of excitonic resonances in NTs has been indicated by several experiments such as 2-photon fluorescence spectroscopy [Wan05] or pump-probe transmission measurements [Kor04]. This work provides additional strong evidence that excitons are the main product of photoexcitation of large-gap tubes.

Remarkably, excitons can also occur in metallic NTs although screening of the e-e interaction is much more effective there. For example, the $(3,3)$ tube turns out to be metallic both in a tight-binding approach and a combined approach based on density-functional theory and many-body perturbation theory [Oni02]. The latter approach, however, additionally predicts 1 bound excitonic state which has a binding energy of ≈ 0.1 eV and is embedded in a continuum of single-electron excitations [Spa04]. Nevertheless, the single-particle picture is expected to remain virtually valid in the small-gap and metallic tubes because screening by free electrons greatly reduces the Coulomb interaction in these systems [Rub05].

5.3.3. Impurity-Induced Carrier Localization

A point-like impurity or defect in a 1-dimensional solid represents a more serious perturbation than in a 3-dimensional solid: As shown in Fig. 5.4, defects in quasi-1-dimensional NTs can lead to the confinement of the electron wavefunction between these defects. Such a localization strongly decreases the dc conductivity of the NT since the conduction electrons have to "hop" over all barriers to get from the start to the end of the 1 dimensional conductor [Dyr00].

Scanning tunneling spectroscopy revealed that the dc conductance of a HiPCO-grown NT decreases *exponentially* as $\exp(-l_{NT}/l_{loc})$ with the NT length l_{NT} rather than linearly [GN05]. This was assigned to the regime of strong Anderson localization and allowed for the extraction of the electronic localization length of $l_{loc} \approx 200$ nm. This value is verified within this work based on simple geometrical arguments.

When electric fields of higher frequencies ω are applied, each electron merely oscillates around a fixed position with a spatial amplitude of $\sim v_F/\omega$ where v_F is the band velocity averaged over the Fermi surface. The defect-induced barriers do *not* play a role any more, if their distance l_{loc} is much larger than this amplitude or, equivalently [Mau94],

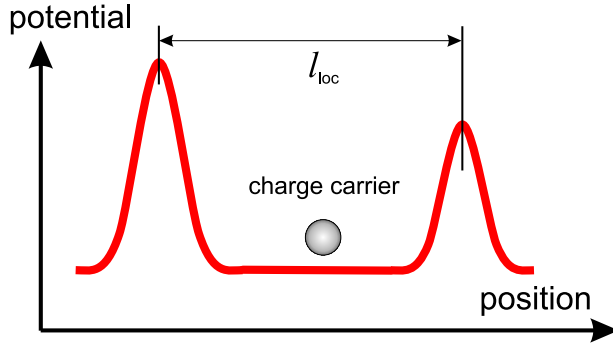$$\omega \gg \omega_{loc} := \frac{v_F}{l_{loc}}.$$

Figure 5.4.: Illustration of localization of a charge carrier between 2 barriers in 1 dimension. The potential barriers are induced by defects or impurities, and the localization length l_{loc} of the electron wavefunction corresponds roughly to the distance between the barriers.

Using $v_{\mathrm{F}} = 10^6\,\mathrm{m\,s^{-1}}$ [Sai98] and $l_{\mathrm{loc}} = 200\,\mathrm{nm}$ [GN05] yields $\omega_{\mathrm{loc}}/2\pi \approx 1\,\mathrm{THz}$ for HiPCO tubes. Far above this frequency, localization effects are not expected to affect the absorption of light. However, it can influence the *real* part of the dielectric function via the Kramers-Kronig relations.

5.4. Phonons

When a graphene sheet is rolled up to a NT, the changed symmetry leads to new fundamental lattice vibrations such as twisting or radial breathing modes [Sai98]. However, the graphene and graphite phonons with their high quantum energies are still present in the resulting NT. Theory even predicts that the strong coupling between the electrons and the high-energy phonons in graphene and graphite is inherent in the NTs as well [Pis04]. As shown for graphite in Chapter 4, these strongly coupled optical phonons (SCOPs) are expected to influence the energy and velocity relaxation of electrons also in NTs substantially. For example, the decrease of the dc conductivity of a metallic NT at high applied electric fields has been attributed to the emission of SCOPs [Jav04, Pop05].

5.5. Optical Properties

The transmission spectrum of a film of bundled NTs is shown in Fig. 5.5. Here. the phonon lines are nearly invisible but show up if the spectrum between 500 and 1900 cm^{-1} is magnified [Kim05]. The broad peak labeled E_{00}^{sg} at $\approx 200\,\mathrm{cm}^{-1}$ has been assigned to optical transitions across the curvature-induced band gap of the small-gap tubes [Itk02, Uga99]. This frequency corresponds to an energy of 25 meV which nicely agrees with measurements of the energy gap of comparable NTs by scanning tunneling spectroscopy [Ouy01].

The peaks E_{11}^{lg}, E_{22}^{lg}, and E_{11}^{sg} in the visible spectral range were first attributed to optical transitions that symmetrically connect the van Hove singularities above and below the Fermi energy in the metallic and small-gap (sg) and large-gap (lg) NTs [Hag03]. However, these peaks rather arise from excitons as has been demonstrated by 2-photon luminescence spectroscopy [Wan05].
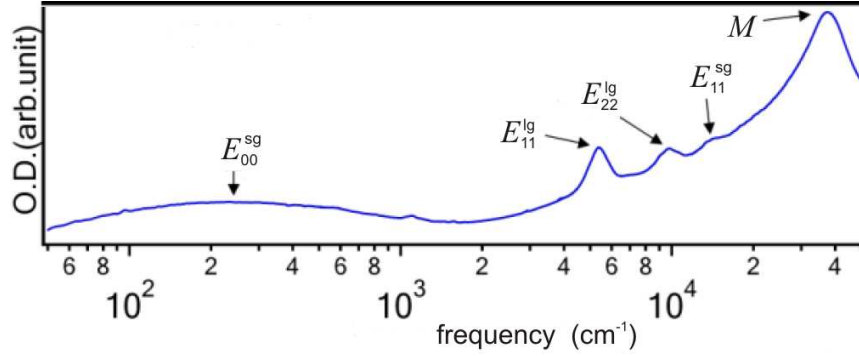
Figure 5.5.: Opical transmission spectrum of a film of bundled NTs taken from Ref. [Kim05]. The range of NT diameters extends from 1.2 to 1.6 nm. Note that $1\,\text{THz} \mathrel{\hat{=}} 33\,\text{cm}^{-1} \mathrel{\hat{=}} 4.1\,\text{meV}$. The various peaks are explained in the text.

The broad peak M is believed to stem from a saddle point in the joint density of states, in analogy to graphene [Kim05].

Another important aspect of the optical properties arises from the large aspect ratio of the NTs: External electric fields *parallel* to the tube axis can polarize a NT much better than fields *perpendicular* to it. As shown in Fig. 5.6, one can consider a NT as a cylinder made of a homogeneous material with susceptibility $\chi_\parallel$ and $\chi_\perp$ parallel and perpendicular to the tube axis, respectively. The electric field $\boldsymbol{E}_{\text{in}}$ *inside* the cylinder is the external macroscopic field $\boldsymbol{E}$ plus an additional field $\boldsymbol{E}_{\text{screen}}$ which tries to screen the external field via the induced polarization $\boldsymbol{P}$ of the cylinder. If all fields involved are homogeneous, one obtains $\boldsymbol{E}_{\text{screen}} = -4\pi L\boldsymbol{P}$ where $L = \text{diag}\left(\frac{1}{2}, \frac{1}{2}, 0\right)$ is the so-called depolarization tensor of the cylinder [Kit96]. Employing $\boldsymbol{P} = \chi\boldsymbol{E}_{\text{in}}$ finally yields [Spa04]

$$\boldsymbol{P}_\parallel = \chi_\parallel \boldsymbol{E}_\parallel \quad \text{and} \quad \boldsymbol{P}_\perp = \frac{\chi_\perp}{1 + 2\pi\chi_\perp}\boldsymbol{E}_\perp$$

which shows that the polarizability perpendicular to the NT axis is greatly reduced if $\chi_\perp > 1$.

The mechanism behind this effect is explained in Fig. 5.6. It has been demonstrated directly by Rayleigh scattering off individual NTs [Sfe04] and is exploited in this work to determine the localization length of the probed electrons.

5.6. Ultrafast Dynamics in Optically Excited Carbon Nanotubes

The charge-carrier dynamics in optically excited NTs has been probed by several techniques such as pump-probe transmission experiments [Man05, She05, Ma05], TRPES [Her00], and time-resolved fluorescence [Hag05b, Wan04]. These experiments employed visible probe
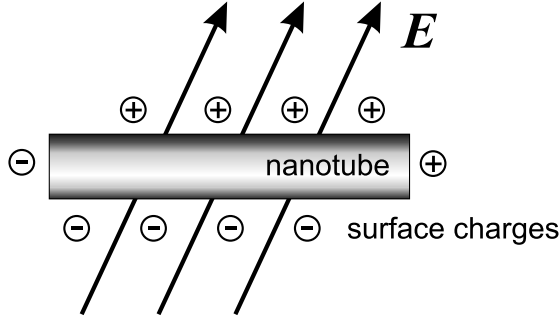
Figure 5.6.: NT in an external macroscopic electric field $\boldsymbol{E}$. The induced polarization $\boldsymbol{P}$ is equivalent to charges on the NT surface which partially screen the external field. For $\boldsymbol{E}$ parallel to the tube axis, the induced positive and negative surface charges are quite distant from each other and thus screen $\boldsymbol{E}$ only weakly. In contrast, if $\boldsymbol{E}$ is perpendicular to the tube axis, the surface charges are quite close to each other which leads to a small field inside the tube and, in turn, to a small polarization in this direction.

pulses and mainly studied the exciton dynamics in large-gap tubes leading to the following picture:

1. As illustrated in Fig. 5.7(a), a pump pulse of appropriate photon energy resonantly populates the excitonic band E_{22}^{lg} in a large-gap tube. The peak of this population rapidly shifts to the E_{11}^{lg} band with a 40-fs time constant followed by efficient energy transfer to strongly coupled optical phonons [Man05, Rub05]. This point will be again discussed in Section 5.9.4.

2. The interaction between two E_{11}^{lg} excitons can lead to the annihilation of the 1st exciton and the promotion of the 2nd exciton to an excited state [Ma05]. The rate of such exciton-exciton annihilation strongly depends on the exciton density and should play a minor role at lower exciton densities. The decay of the remaining excitons is not yet completely clear but time-resolved fluorescence suggests that defect-induced trap states play an important role in this process [Hag05b].

3. In NT bundles, an additional effective decay channel opens up: E_{11}^{lg} excitons can tunnel into adjacent small-gap and metallic tubes where the resulting electrons and holes relax efficiently via phonon emission. This is suggested by the absence of fluorescence from NT bundles [O'C02, She05].

However, there are much less reports on the dynamics in small-gap and metallic tubes: Probing NT mats by time-resolved photoemission spectroscopy (TRPES) also revealed dynamics on a subpicosecond- and picosecond-time scale. Remarkably, although not explicitly mentioned in that report, a loss of $\approx 90\,\%$ of the energy of the excited electrons within $0.5\,\mathrm{ps}$ was found in Ref. [Hag04] in complete analogy to the findings in Chapter 4. This is not surprising in view of the the strongly coupled optical phonons of graphite which are also present in NTs, see Section 5.4.

Figure 5.7.: (a) Excitation scheme of a large-gap NT. The pump pulse resonantly populates the 2nd excitonic band E_{22}^{lg}. (b) Excitation and probing scheme of a small-gap NT together with a magnification of the region around the Fermi edge. The pump pulse creates electrons and holes which subsequently relax to the vicinity of the small gap. The different electronic occupation numbers are represented by various gray scales.
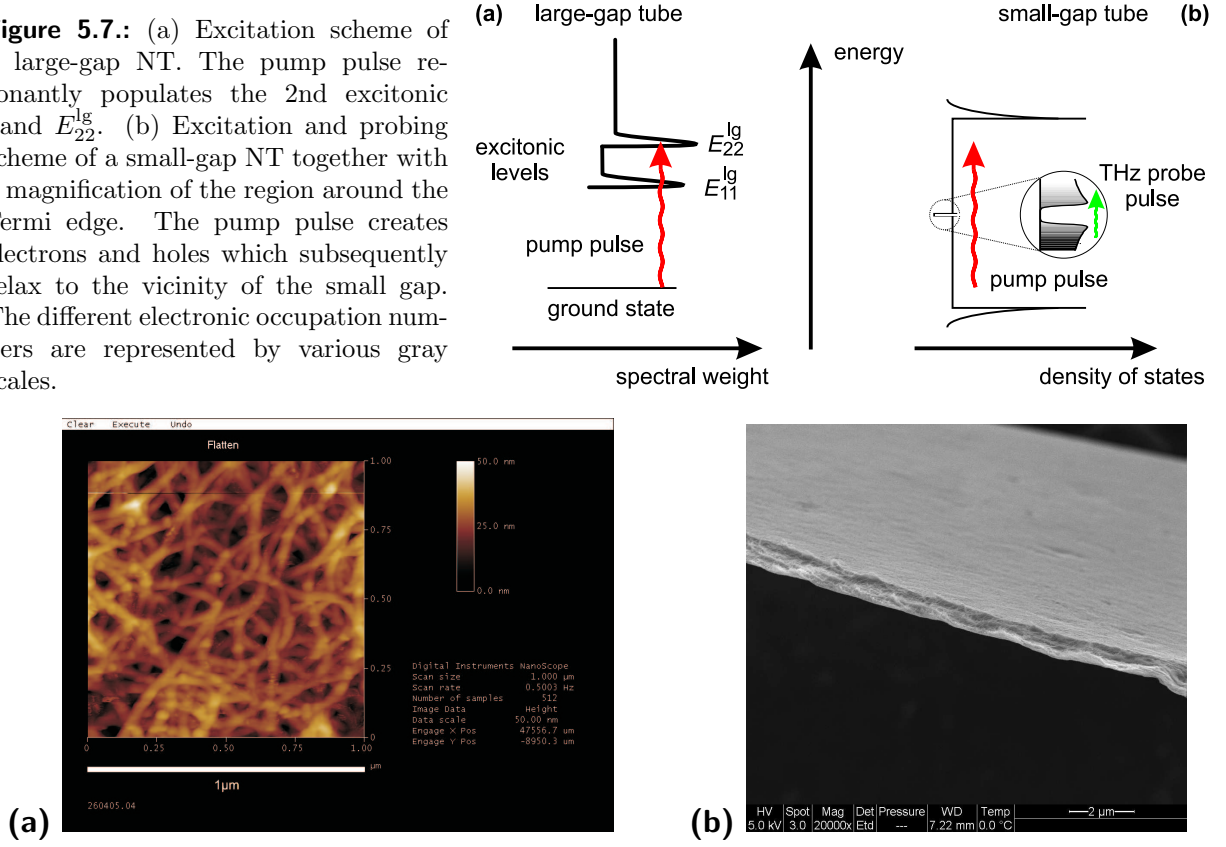

Figure 5.8.: (a) Topography of the NT sample taken with an atomic force microscope. The image reveals that the NT axes are bent with a mean radius of curvature of $\sim 100\,\text{nm}$. (b) Side view of the NT film obtained by scanning electron microscopy. The thickness of the film is about $800\,\text{nm}$. The images have been provided by Carla Aguirre (École Polytechnique de Montréal).

5.7. Experimental and Technical Details

5.7.1. Sample Preparation

The NT sample was prepared by Carla Aguirre (École Polytechnique de Montréal) similar to the procedure described in Ref. [Wu04]. First, HiPCO NTs (Tubes@Rice) are dispersed in a 2-% sodium-cholate solution. Centrifuging results in a supernatant that is used to produce a suspension that contains a substantial amount of isolated NTs surrounded by sodium cholate molecules. After vacuum-filtering onto a filtration membrane and washing away the surfactant with purified water, the membrane is dissolved, and the remaining NT film is transferred to a diamond substrate. Finally, the film is annealed at $600\,°\text{C}$ under a constant flow of argon for 1 hour to remove most of the remaining contaminants.

Figure 5.8(a) shows an image of the sample surface taken by an atomic force microscope. Note that the NT axes are *bent* with a mean radius of curvature of $100\,\text{nm}$. Moreover, the NTs are preferentially oriented parallel to the sample surface and, to some extent, isolated
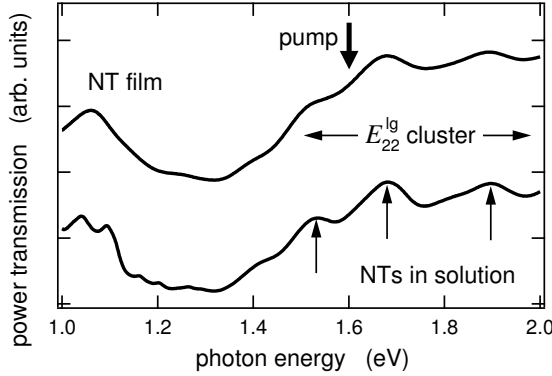
Figure 5.9.: Optical transmission spectrum between 1 and 2 eV of the NT film investigated and the NT solution the film is made from. Thin arrows mark E_{22}^{lg} resonances of various tube types contained in the film. The thick vertical arrow marks the mean photon energy of the pump pulse which is located in the E_{22}^{lg} exciton band. The transmission data have been provided by Carla Aguirre (École Polytechnique de Montréal).

from each other. Figure 5.8(b) has been obtained by scanning electron microscopy and reveals that the NT film has a thickness of $d \approx 800$ nm. The sample contains *all types of nanotubes* with a diameter distribution that extends from about 0.8 to 1.2 nm [Hag03].

The optical transmission spectrum of the NT film in Fig. 5.9 looks quite similar to that of the NT solution the film is made from. In particular, the E_{22}^{lg} excitonic resonances of the various tube types are still but less visible which is due to a higher degree of tube bundling [Hag05a]. Figure 5.9 also shows that the pump photon energy is located directly in the E_{22}^{lg} cluster.

The power transmission of the NT film at an 800-nm wavelength is $T = 0.25$. It can be used to estimate the space filling factor F of the NTs since it is related to the number density n_{C} of the C atoms by $T = \exp(-\alpha n_{\mathrm{C}} d)$ with $\alpha \approx 0.5 \cdot 10^6\,\mathrm{cm^2\,mol^{-1}}$ [Isl04]. The resulting density $n_{\mathrm{C}} = 0.035\,\mathrm{mol\,cm^{-3}}$ is a factor $F = 0.27$ less than the theoretical close-packing density of $0.13\,\mathrm{mol\,cm^{-3}}$ of NTs with a 1-nm diameter [Sai98].

5.7.2. Sample Pumping and Probing

The pump-and-probe geometry of the NT sample is the same as that of the graphite sample as described in Section 4.6.2. Note that the NT film is substantially thicker than the penetration depth of the pump pulse since the power transmission of the sample is only $T = 0.25$. Although leading to an inhomogeneous excitation profile, this is not a complication here: In contrast to graphite in Section 4.6.2, ultrafast transport processes into the depth of the NT film are not expected since the NTs are preferentially oriented parallel to the sample surface. Therefore, the excitation profile (4.5) does not change on the picosecond scale which is the time scale of interest here.

The probe polarization is parallel to the optical table which corresponds to the x axis in Fig. 5.10(b). Probing the sample along the y direction was achieved by keeping the probe polarization along x and instead turning the pump polarization by 90°.
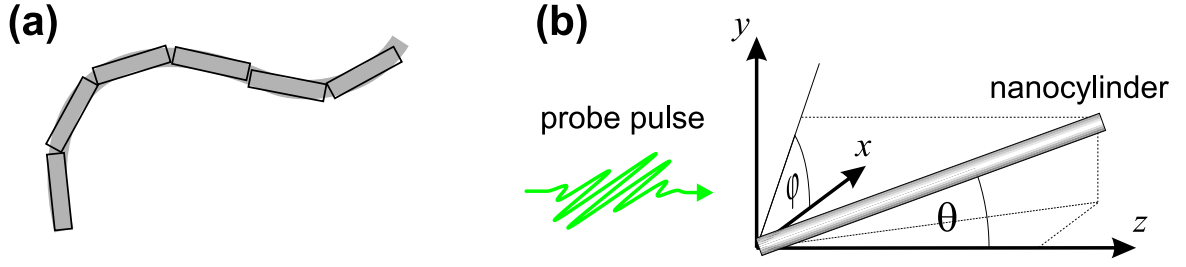
(a)

(b)

Figure 5.10.: (a) A bent NT can be understood as a chain of nanocylinders (NCs). (b) The orientation of a NC in the reference frame is determined by 2 angles, the azimuth φ and the zenith θ. In the experiment, both pump and probe beam propagate along the z axis, that is normally to the sample surface. The probe beam is polarized along the x axis, whereas the pump beam is either polarized along the x or y axis.

5.7.3. Data Analysis

The NT film investigated here consists of nanoparticles that are embedded in a host material. Therefore, its dielectric function varies on a microscopic length scale, and the relation to the measured quantities in THz spectroscopy is more involved. Moreover, the NTs are bent, and there are different types of NTs with different optical properties. The situation becomes even more complicated after excitation by a pump pulse which produces additional anisotropies and inhomogeneities.

However, as mentioned in Section 1.4.1, the macroscopic optical polarization $\boldsymbol{P}$ is obtained by spatially averaging the microscopic polarization over a length scale l_{avg}. Since many NTs are contained in the averaging volume $V_{\mathrm{avg}} = l_{\mathrm{avg}}^3$, the probe light "sees" an effectively homogeneous and isotropic sample with an effective susceptibility χ^{eff}. This is the basis of the so-called effective medium approach.

In order to derive the effective susceptibility of both the unexcited and excited NT film, we consider a long bent NT as a chain of independent short straight nanocylinders (NCs) as shown in Fig. 5.10(a). If the relevant length scales fulfill the relation

$$\text{radius of curvature of bent NT} \gg \text{NC length} \gg \text{NT diameter},$$

each NC can be considered as a NT with corresponding properties. This condition is certainly fulfilled for a cylinder length of, for instance, $20\,\mathrm{nm}$. Moreover, the NCs are assumed to be oriented randomly.

Steady State

The NT film is made of various sorts of NCs. Each sort s occupies the volume fraction F^s and has the diagonal susceptibility tensor $\chi^s = \mathrm{diag}\left(\chi_{\parallel}^s, \chi_{\perp}^s, \chi_{\perp}^s\right)$ where $\chi_{\parallel}^s$ and $\chi_{\perp}^s$ are the susceptibilities parallel and perpendicular to the NC axis. The depolarization tensor of this NC is simultaneously diagonal, $L^s = \mathrm{diag}\left(\frac{1}{2}, \frac{1}{2}, 0\right)$ [Kit96]. The host material "h"

filling the space between the NCs is assumed to consist of spheres with scalar susceptibility χ^{h} and depolarization tensor $L^{\mathrm{h}} = \mathrm{diag}\left(\frac{1}{3}, \frac{1}{3}, \frac{1}{3}\right)$ [Kit96]. Then the effective-medium approximation results in an equation for the effective *scalar* susceptibility χ^{eff} [Noh91],

$$9(F-1)\frac{\chi^{\mathrm{eff}}-\chi^{\mathrm{h}}}{2\chi^{\mathrm{eff}}+\chi^{\mathrm{h}}} = \sum_s F^s \left(4\frac{\chi^{\mathrm{eff}}-\chi^s_{\perp}}{\chi^{\mathrm{eff}}+\chi^s_{\perp}} - \frac{\chi^s_{\parallel}}{\chi^{\mathrm{eff}}} + 1\right). \tag{5.1}$$

We assume the host material to be air with $\chi^{\mathrm{h}} \approx 0$. If the total NT volume fraction $F = \sum F^s$ is small, $F \ll 1$, the effective susceptibility is comparable to that of the host and thus small compared to the susceptibilities $\chi^s_{\parallel}$ and $\chi^s_{\perp}$, $|\chi^{\mathrm{eff}}| \sim |\chi^{\mathrm{h}}| \ll |\chi^s_{\perp}| \sim |\chi^s_{\parallel}|$. In this case, the 1st term on the right-hand side of Eq. (5.1) is ≈ -4 which leads to

$$F\frac{\langle\chi_{\parallel}\rangle}{\chi^{\mathrm{eff}}} = -3F + 9(1-F)\frac{\chi^{\mathrm{eff}}-\chi^{\mathrm{h}}}{2\chi^{\mathrm{eff}}+\chi^{\mathrm{h}}}.$$

Here, $\langle\chi_{\parallel}\rangle = \sum F^s \chi^s_{\parallel}/F$ is the susceptibility parallel to the nanotube axis averaged over all nanotubes. As expected from the depolarization effects, $\chi_{\perp}$ does not contribute here, but is not negligible for larger F since the assumption $|\chi^{\mathrm{eff}}| \ll |\chi^s_{\perp}| \sim |\chi^s_{\parallel}|$ is not valid any more. This is most likely due to NT bundling at higher NT volume fractions: A thick NT bundle has a larger polarizability perpendicular to the tube axis than a single thin NT as detailed in Section 5.5.

Again assuming once more $F \ll 1$ and in addition $\chi^{\mathrm{eff}} \approx \chi^{\mathrm{h}}$ yields the intuitive result

$$\chi^{\mathrm{eff}} - \chi^{\mathrm{h}} = \frac{1}{3}F\langle\chi_{\parallel}\rangle \tag{5.2}$$

for the effective susceptibility χ^{eff}: The change of the polarizability of the host medium is proportional to that of the NTs times the volume fraction of the NTs. The factor of $1/3$ arises since the NT is polarizable along only 1 of all 3 spatial dimensions. Small changes in the prefactor of $1/3$ are possible since the NTs in our sample lie mainly parallel to the substrate surface and are therefore not completely randomly oriented. Moreover, the assumption $\chi^{\mathrm{eff}} \approx \chi^{\mathrm{h}}$ is not valid here; instead one has $|\chi_{\parallel}| \gg |\chi^{\mathrm{eff}}| \gg |\chi^{\mathrm{h}}|$ which also modifies the prefactor. However, these changes are small and not relevant for the conclusions of this chapter.

The effective dielectric function $\varepsilon^{\mathrm{eff}} = 1 + 4\pi\chi^{\mathrm{eff}}$ of our NT film is obtained from the experimental data analog to graphite in Section 4.6.3; one just has to replace ε by $\varepsilon^{\mathrm{eff}}$. Equation (5.2) provides the relation between χ^{eff} and $\langle\chi_{\parallel}\rangle$.

Excited Sample

After sample excitation by the pump pulse, the susceptibility tensor of the NT network changes by $\Delta\chi(\boldsymbol{x})$. This results in a change $\Delta\boldsymbol{p}$ of the NC dipole moment $\boldsymbol{p}$ induced by the probe field $\boldsymbol{E}_{\mathrm{in}}$ *inside* the NC via

$$\Delta\boldsymbol{p} = V_{\mathrm{NC}}\Delta\chi\boldsymbol{E}_{\mathrm{in}} \overset{(\mathrm{i})}{\approx} V_{\mathrm{NC}}\Delta\chi_{\boldsymbol{e}}\boldsymbol{E}_{\mathrm{in}\boldsymbol{e}} \overset{(\mathrm{ii})}{\approx} V_{\mathrm{NC}}\Delta\chi_{\boldsymbol{e}}\boldsymbol{E}_{\boldsymbol{e}}$$

where V_{NC} is the volume of the NC at position $\boldsymbol{x}$. In step (i), we exploited that only the field component $\boldsymbol{E_e} = (\boldsymbol{eE})\boldsymbol{e}$ parallel to the axis direction

$$\boldsymbol{e} = \boldsymbol{e}(\theta, \varphi) = \begin{pmatrix} \cos\varphi \sin\theta \\ \sin\varphi \sin\theta \\ \cos\theta \end{pmatrix}$$

of the NC in Fig. 5.10(b) makes the major contribution to the pump-induced polarization change. In step (ii) we employed $\boldsymbol{E}_{\mathrm{in}\boldsymbol{e}} = \boldsymbol{E_e}$ since depolarization effects along the NC axis are negligible, see Section 5.5.

Averaging over all NCs in the volume $V_{\mathrm{avg}}(\boldsymbol{x})$ around position $\boldsymbol{x}$ yields the pump-induced change in the polarization,

$$\boldsymbol{P}_{\mathrm{NL}}(\boldsymbol{x}) = \frac{1}{V_{\mathrm{avg}}(\boldsymbol{x})} \sum_{\boldsymbol{x}_j \in V_{\mathrm{avg}}(\boldsymbol{x})} \Delta\boldsymbol{p}_j = \frac{\boldsymbol{E}(\boldsymbol{x})}{V_{\mathrm{avg}}(\boldsymbol{x})} \sum_j V_{\mathrm{NC}} \Delta\chi_{\boldsymbol{e}}(\boldsymbol{x}_j)\, \boldsymbol{e}_j\,{}^{\mathrm{t}}\boldsymbol{e}_j,$$

where j numbers the NCs. One can now split the j summation in an integration $\int |\mathrm{d}\Omega|$ over all solid angles $\mathrm{d}\Omega = \mathrm{d}\varphi\, \mathrm{d}\cos\theta$ and a summation $\sum_{j'}$ over a subset of NCs j' whose orientation $\boldsymbol{e}$ points to the solid angle $\mathrm{d}\Omega$. The latter summation yields

$$\sum_{j'} V_{\mathrm{NC}} \Delta\chi_{\boldsymbol{e}}(\boldsymbol{x}_{j'}) = \Delta\chi_{\boldsymbol{e}}(\boldsymbol{x}) \cdot F V_{\mathrm{avg}} \cdot w(\boldsymbol{e})\, |\mathrm{d}\Omega|$$

where $w(\boldsymbol{e})\, |\mathrm{d}\Omega|$ is the probability of the $\boldsymbol{e}$ subset, and $\Delta\chi_{\boldsymbol{e}}(\boldsymbol{x})$ is its mean change in susceptibility. One then obtains

$$\boldsymbol{P}_{\mathrm{NL}}(\boldsymbol{x}, \omega) = F\boldsymbol{E}(\boldsymbol{x}, \omega) \int |\mathrm{d}\Omega|\, w(\boldsymbol{e}) \Delta\chi_{\boldsymbol{e}}(\boldsymbol{x})\, \boldsymbol{e}\,{}^{\mathrm{t}}\boldsymbol{e}.$$

Since the probe beam is polarized along the x axis in Fig. 5.10(b), one can exploit the invariance of $w(\boldsymbol{e})\Delta\chi_{\boldsymbol{e}}$ with respect to the transformation $\theta \longrightarrow -\theta$ which enforces $P_{\mathrm{NL}z} = 0$. Moreover, if the pump polarization is parallel or perpendicular to the probe polarization, this invariance also holds for the transformation $\varphi \longrightarrow -\varphi$ implying $P_{\mathrm{NL}y} = 0$. Therefore, the polarization change is parallel to the probe polarization, and the pump-induced change in the effective susceptibility finally is

$$\Delta\chi_{ij}^{\mathrm{eff}} = 0 \quad \text{for} \quad i \neq j$$

and

$$\Delta\chi_{xx}^{\mathrm{eff}}(\boldsymbol{x}) = F \int |\mathrm{d}\Omega|\, w(\boldsymbol{e})\, \Delta\chi_{\boldsymbol{e}}(\boldsymbol{x})\, \sin^2\theta \cos^2\varphi. \tag{5.3a}$$

This result reflects the expectation that we mainly probe tubes parallel to the probe polarization that is $\varphi = 0$ and $\theta = 90°$ in Fig. 5.10(b). The angular factor in the last expression arises because the probe field induces a dipole moment along the NC axis which involves a
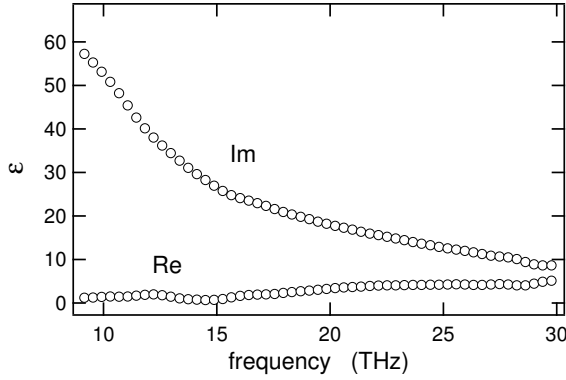
Figure 5.11.: Measured dielectric function (5.4) of the NT sample between 9 and 30 THz and averaged over all NT types and orientations. The increase of $\mathrm{Im}\,\varepsilon$ towards lower frequencies originates from the broad resonance at $\approx 6\,\mathrm{THz}$ in Fig. 5.5.

factor $\sin\theta\cos\varphi$. Since this dipole moment is observed along the probe polarization, one has to project back onto this direction and gets another factor $\sin\theta\cos\varphi$.

The component $\Delta\chi_{yy}^{\mathrm{eff}}$ is simply obtained by replacing $\cos\varphi$ in Eq. (5.3a) by $\sin\varphi$,

$$\Delta\chi_{yy}^{\mathrm{eff}}(\boldsymbol{x}) = F\int|\mathrm{d}\Omega|\,w(\boldsymbol{e})\,\Delta\chi_{\boldsymbol{e}}(\boldsymbol{x})\,\sin^2\theta\sin^2\varphi, \qquad (5.3\mathrm{b})$$

which can be different from the xx component. Such pump-induced optical anisotropy will be discussed in Section 5.9.2. Therefore, it is important to have the pump and probe polarizations either parallel or perpendicular to each other. Otherwise, the sample can cause a rotation or ellipticity of the probe polarization whose electro-optic detection will lead to more complicated results [Pla01].

In order to check the validity of the above derivation, we assume a completely isotropic and homogeneous $\Delta\chi_{\boldsymbol{e}}(\boldsymbol{x}) = \Delta\chi_{\parallel}$ and an isotropic distribution of the tube directions, $w(\boldsymbol{e}) = 1/4\pi$. This yields $\Delta\chi_{xx}^{\mathrm{eff}} = \Delta\chi_{yy}^{\mathrm{eff}} = \frac{1}{3}F\Delta\chi_{\parallel}$ in agreement with Eq. (5.2).

At the pump beam intensities in our experiment, $\Delta\chi_{xx}^{\mathrm{eff}}(z)$ is due to a 1-photon absorption and therefore decays exponentially as $\Delta\chi_{xx}^{\mathrm{eff}}(z) = \Delta\chi_{xx}^{\mathrm{eff}}(z=0^+)\exp(-z/d_{\mathrm{pen}})$ along the z axis in Fig. 5.10(b). The penetration depth $d_{\mathrm{pen}} = 580\,\mathrm{nm}$ is derived from the sample thickness and the sample power transmission of $T = 0.25$. The extraction of the susceptibility $\Delta\chi_{xx}^{\mathrm{eff}}(z=0^+)$ directly behind the film surface is now straightforward with the aid of Eq. (2.16). Note that one has to use the *effective* susceptibility χ^{eff} for the unexcited sample.

5.8. Results: Unexcited Sample

Figure 5.11 presents the quantity

$$\varepsilon := \frac{4\pi}{F}(\chi^{\mathrm{eff}} - \chi^{\mathrm{h}}). \qquad (5.4)$$

According to Equation (5.2), ε is the dielectric function of the unexcited NTs between 9 and 30 THz averaged over all NT types and orientations.

Contributions from the large-gap tubes are not expected since their excitation energies in the ground state are on the eV scale and thus exceed our probe-photon energies by far. The increase of $\mathrm{Im}\,\varepsilon$ towards low frequencies arises from the broad resonance E_{00}^{sg} centered at about 6 THz in Fig. 5.5. As mentioned above, this feature has been attributed to optical transitions across the gap of the small-gap NTs [Itk02, Uga99].

Moreover, ε does not display a distinct free-carrier response which would imply a large negative real part as described in Section 1.6.1. The negligibly small $\mathrm{Re}\,\varepsilon$ is consistent with the low plasma frequency of $\hbar\Omega_{\mathrm{pl}} \approx 20\,\mathrm{meV}$ found in metallic and small-gap tubes by conductivity measurements below 5 THz [Hil00, Krö05]. A possible reason for this behavior might be the localization of charge carriers which decreases the conductivity at least below a characteristic frequency, see Section 5.3.3.

5.9. Results: Excited Sample

We now consider the changes in the dielectric function of the NT sample after pump pulse excitation with an incident fluence of $30\,\mu\mathrm{J\,cm^{-2}}$. From the absorption cross sections for 1.6-eV photons [Isl04], we estimate that $\sim 10^{-4}$ photons per carbon atom are absorbed close to the front surface of the NT sample. This excitation density is comparable to that of graphite in Section 4.8.

The pump-induced change in the dielectric function plotted in the following is defined as

$$\Delta\varepsilon_{xx,\tau} := \frac{4\pi}{F}\Delta\chi_{xx,\tau}^{\mathrm{eff}}(z = 0^+).$$

According to Eq. (5.3a), $\Delta\varepsilon_{xx,\tau}$ describes an excited NT directly behind the sample surface and averaged over all possible NT types and directions. If not otherwise mentioned, the xx component, that is the component along the pump polarization, is considered.

All types of NTs are excited by the 1.6-eV pump pulse as sketched in Fig. 5.7. Transient transmission measurements with pump-photon energies *above and below* the E_{11}^{lg} band indicate that roughly half of the absorbed 1.6-eV pump photons resonantly populate the E_{22}^{lg}-exciton bands of the large-gap tubes [Ell05]. The remaining portion resonantly excites the small-gap and metallic NTs.

5.9.1. No Response of Free Charge Carriers

Figure 5.12(a) shows $\Delta\varepsilon_\tau$ for 3 different pump-probe delays τ. Note that $\Delta\varepsilon_\tau$ is quite small and does *not* exhibit a distinct free-carrier response. This is in striking contrast to the model semiconductor GaAs, where excitation above the band gap creates electrons and holes [Hub01], and to graphite, which is closely related to NTs: Its corresponding $\Delta\varepsilon_\tau$ taken under comparable excitation conditions (see above) is plotted in Fig. 5.12(a) for
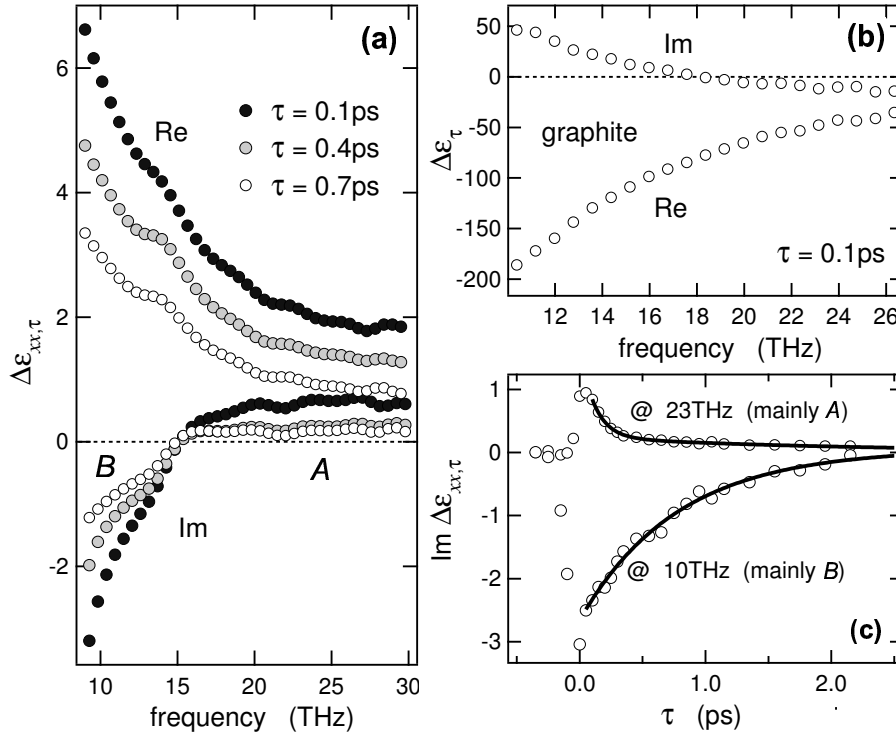
Figure 5.12.: (a) Pump-induced changes in the NT dielectric function for several pump-probe delays τ. In the imaginary part, the absorption and bleaching feature are labeled A and B, respectively. (b) As reference, the pump-induced changes in the dielectric function of highly oriented pyrolytic graphite at $\tau = 0.1\,\text{ps}$ after excitation with comparable strength as in the NT measurements. Note the different scales of the ordinates. (c) Temporal decay of $\text{Im}\,\Delta\varepsilon_\tau$ at $10\,\text{THz}$ (mainly feature B) and $23\,\text{THz}$ (mainly feature A). The decay of B is well described by a single-exponential with a time constant of $0.9\,\text{ps}$ whereas the decay of A is fitted best to a double-exponential with time constants of $0.15\,\text{ps}$ and $4.3\,\text{ps}$, respectively.

$\tau = 0.1\,\text{ps}$. The 2 orders of magnitude larger and negative $\text{Re}\,\Delta\varepsilon_\tau$ is a clear signature of free charge carriers, and the lack of such a response from the NT sample has important consequences:

- It strongly supports the assertion that excitons are the main products of photoexcitation of large-gap tubes [Man05, Kor04]. These strongly bound electron-hole pairs are not directly visible in our experiment since their internal excitation energies of $0.2\,\text{eV}$ [Wan05] exceed our probe energies of $\sim 50\,\text{meV}$ by far.

- The plasma frequency and the Drude scattering rate in the small-gap and metallic NTs do not change appreciably upon excitation. This can be traced back to Eq. (1.22) and to their peculiar eDOS as detailed in Fig. 5.13. An example of the opposite behavior is graphite in Section 4.8.3.

Figure 5.13.: Electronic density of states $D(\epsilon)$ in a small-gap NT with an energy gap of $20\,\mathrm{meV}$ and derivative $-\partial f/\partial\epsilon$ of the Fermi function at an electronic temperature of $T_\mathrm{e} = 300\,\mathrm{K}$. The width of $-\partial f/\partial\epsilon$ increases with rising T_e and is much larger than the energy gap. As a consequence, the squared plasma frequency Ω_pl^2, which is the area under the product curve $-D(\epsilon)\cdot\partial f/\partial\epsilon$, changes only weakly.
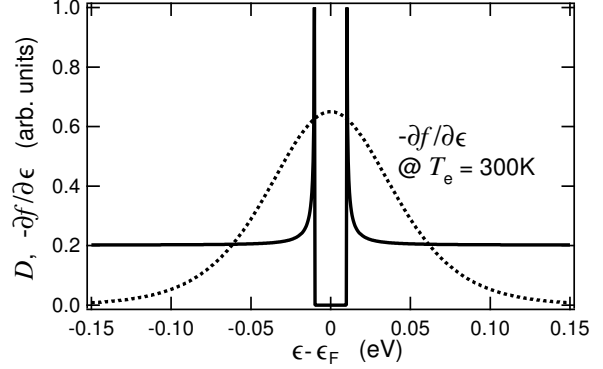
5.9.2. Pump-Induced Anisotropy and Carrier Localization

To identify the origin of the pump-induced signal, we now analyze the spectral structure of our data in Fig. 5.12(a): $\mathrm{Im}\,\Delta\varepsilon_\tau$ is positive above $15\,\mathrm{THz}$, which implies increased light absorption accordingly labeled "A". In contrast, $\mathrm{Im}\,\Delta\varepsilon_\tau$ is negative below $15\,\mathrm{THz}$, which means decreased light absorption (bleaching) and is labeled "B". The following arguments strongly indicate that A and B arise from distinct products in the photoexcited NTs:

- A and B exhibit significantly different temporal decays as can be seen in Fig. 5.12(c): At early times, A decreases much faster than B.

- A and B respond differently to a change in the probe pulse polarization as shown in Fig. 5.14(a,b): The pump-induced dichroism

$$D_\tau = \frac{\mathrm{Im}\,\Delta\varepsilon_{xx,\tau}}{\mathrm{Im}\,\Delta\varepsilon_{yy,\tau}} = \frac{\mathrm{Im}\,\Delta\chi_{xx,\tau}^{\mathrm{eff}}}{\mathrm{Im}\,\Delta\chi_{yy,\tau}^{\mathrm{eff}}} \tag{5.5}$$

is found to be $\approx 1.2 \pm 0.1$ for feature B but $\approx 2.1 \pm 0.2$ for feature A.

Such transient optical anisotropy has previously been observed for visible probe pulses [She05] and relies on the greatly reduced NT polarizability perpendicular to the tube axis, see Section 5.5. Therefore, and as illustrated in Fig. 5.15, the probe pulse is most sensitive to tubes parallel to the probe polarization. Likewise, the pump pulse is absorbed most effectively by tubes parallel to the pump polarization. As a consequence, parallel pump and probe polarizations should give a larger pump-induced signal than in the perpendicular case.

This effect is largest if the pump-induced excitations have a spatial extent much smaller than the mean radius of curvature $R_\mathrm{c} \sim 100\,\mathrm{nm}$ of the bent NT, see Fig. 5.8(a). On the other hand, a dichroism of 1 is attained when the excitations are spatially delocalized with respect to R_c. Therefore, the pump-induced dichroism of A and B provides *direct* evidence of the existence of localized and delocalized electrons in the bent NTs.
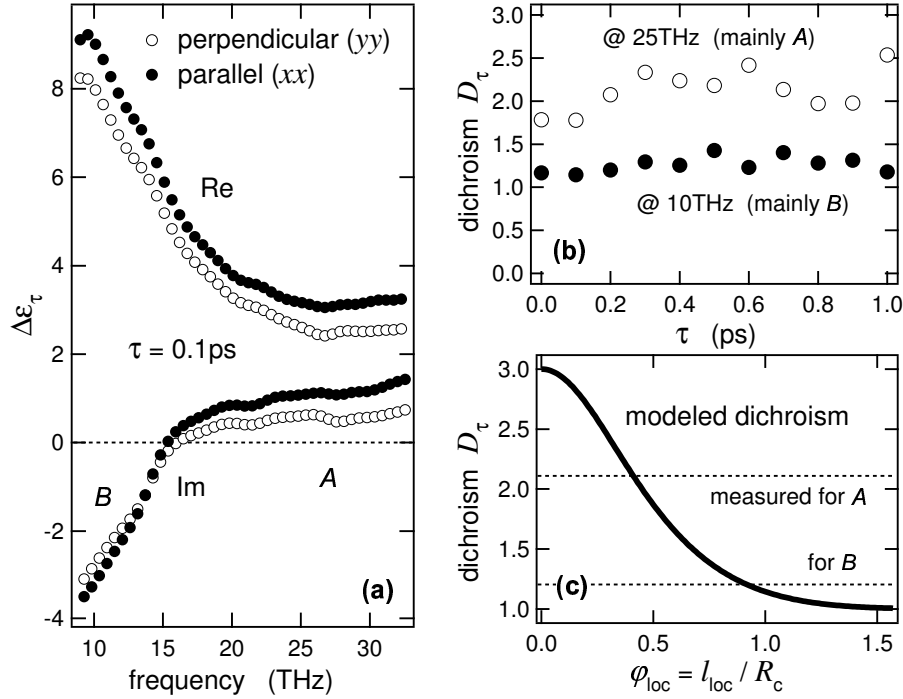
Figure 5.14.: (a) Dielectric function at $\tau = 0.1\,\text{ps}$ parallel (xx) and perpendicular (yy) to the pump polarization. The difference between the xx and yy curves directly shows the pump-induced optical anisotropy. It is most pronounced in the imaginary part above $20\,\text{THz}$ where feature A dominates. Such dichroism is a direct consequence of excitations in the NTs which are localized on a length scale smaller than the radius of curvature of the bent tube. (b) Temporal dynamics of the pump-induced dichroism (5.5) at $10\,\text{THz}$ (mainly feature B) and $25\,\text{THz}$ (mainly feature A). (c) Expected pump-induced dichroism as a function of the localization length of the corresponding excitation. Lines mark the measured dichroism of feature A and B.

Estimate of the Electron Localization Length

In order to estimate the localization length of the electrons, we assume the NTs to be bent to circles with radius R_c as shown in Fig. 5.15(b). Moreover, they are assumed to be parallel to the (x, y) plane defined in Fig. 5.10. In other words, the orientational distribution of the nanocylinders is

$$w(\boldsymbol{e}) = w(\theta, \varphi) \propto \delta(\theta - 90°).$$

Exciting the NTs with a pump-beam polarization along the x axis will induce a susceptibility change $\Delta\chi_{\boldsymbol{e}} = \Delta\chi_\varphi \propto \cos^2\varphi$ provided the excited carriers are perfectly localized. However, a finite localization length l_loc leads to a "smearing" or convolution (B.2) of the carrier position by a function of width l_loc. Equivalently, $\Delta\chi_\varphi$ is convolved by a function $s(\varphi)$ of width $\varphi_\text{loc} = l_\text{loc}/R_\text{c}$ which leads to an angular distribution $\Delta\chi_\varphi \propto \cos^2\varphi * s(\varphi)$. When the smearing s has Gaussian shape, $s(\varphi) = \exp(-\varphi^2/2\varphi_\text{loc}^2)$, the change in the effective susceptibilities (5.3) parallel and perpendicular to the pump polarization can be
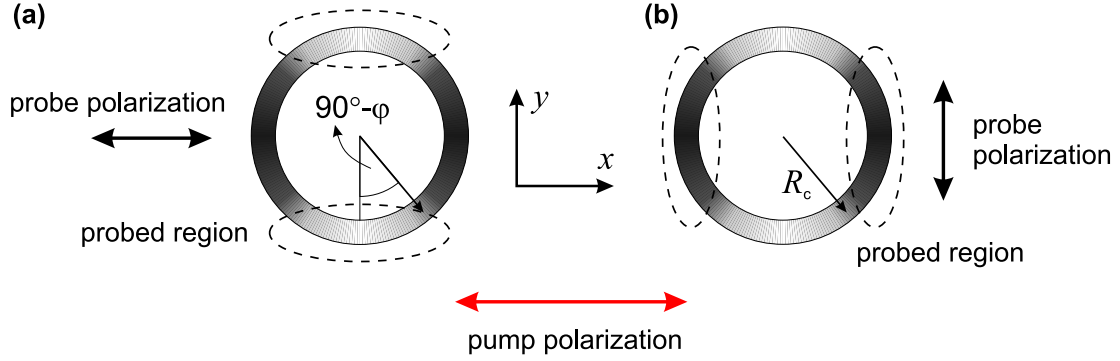
Figure 5.15.: Illustration of the origin of the pump-induced anisotropy. The pump beam mainly excites tube segments parallel to its polarization along the x direction. These segments are drawn brighter than the less strongly excited regions. Similarly, the probe beam is most sensitive to tube segments parallel to its polarization. (a) Parallel pump and probe polarization. The probe pulse is most sensitive to the tube segments with a maximum change in the susceptibility provided the pump-induced excitations are localized with respect to the tube radius of curvature R_c. (b) Perpendicular pump and probe polarization. The probe beam is most sensitive to the less excited tube segments and therefore less affected by the pump-induced changes than in case (a).

calculated analytically and yields

$$\left.\begin{array}{c}\Delta\chi_{xx}^{\mathrm{eff}}\\\Delta\chi_{yy}^{\mathrm{eff}}\end{array}\right\}\propto\Delta\chi_{\varphi=0}\left[2\pm\exp(-2\varphi_{\mathrm{loc}}^2)\right].$$

Here, $\Delta\chi_{\varphi=0}$ is the susceptibility change of the NT segments parallel to the pump polarization. The resulting pump-induced dichroism (5.5) becomes

$$D_\tau=\frac{2+\exp(-2\varphi_{\mathrm{loc}}^2)}{2-\exp(-2\varphi_{\mathrm{loc}}^2)} \tag{5.6}$$

which is plotted in Fig. 5.14(c).

As expected, a complete delocalization with $\varphi_{\mathrm{loc}}=0$ implies a dichroism of 1, whereas perfect localization with $\varphi_{\mathrm{loc}}=\infty$ leads to a a dichroism of 3. As to our data in Fig. 5.14(b), the excitations correlated with feature A have a localization length of $\approx0.4R_\mathrm{c}\sim40\,\mathrm{nm}$ and are substantially more localized than those related to feature B having a twice as large localization length of $\approx0.9R_\mathrm{c}\sim90\,\mathrm{nm}$. The localization lengths found here agree reasonably with those extracted by scanning tunneling spectroscopy of HiPCO NTs [GN05]. Note that the transient dichroism remains constant in Fig. 5.14(b) showing that carrier transport is negligible during the 1st picosecond after sample excitation.

It should be mentioned that the derivation of Eq. (5.6) assumes that only 1 type of excitations induces the pump-induced signal whereas in our case at least 2 types, namely A and B, contribute. However, B completely dominates the signal at $10\,\mathrm{THz}$ since the dichroism still remains at ≈1.2 when A has already reduced to small values. Conversely, B has only little spectral weight above $25\,\mathrm{THz}$ and thus does not interfere with feature A in this spectral region.

To summarize, the pump-induced dichroism allows for a direct observation of pump-induced excitations A and B that are localized and delocalized with respect to a length scale of $\sim 100\,\text{nm}$. The dichroism is based on the greatly reduced polarizability of the NTs perpendicular to the tube axis whereas the spatial resolution comes into play due to the radius of curvature of the bent NTs. The remaining sections are dedicated to a discussion of the origin of A and B.

5.9.3. Bleaching in Small-Gap Tubes

Phononic contributions as a cause of the bleaching feature B are excluded, since broad phonon bands are neither predicted [Ye04] nor observed [Kim05] in the probed spectral region. Consequently, B must arise from electronic transitions. Stimulated emission from excited excitonic levels in large-gap tubes can be ruled out because the lowest E_{11}^{lg} state is attained within 40 fs after optical excitation [Man05]. We conclude that B is due to metallic and small-gap tubes.

The single-electron approach in Fig. 5.7(b) can qualitatively explain the observed effect: After pump pulse absorption, the excited electrons thermalize to a Fermi-Dirac distribution within $\approx 0.2\,\text{ps}$ [Her00]. This results in additional electrons and holes around the Fermi energy. Similar to graphite in Section 4.8.2, these hot carriers block originally possible optical transitions connecting the van Hove singularities near the band gap. The contributions of various tube types lead to an inhomogeneously broadened bleaching feature B as seen in our experiment [Shy02].

Similar to graphite in Section 4.8.4, the small Fermi surface and the strong e-ph interaction suggest a very rapid cooling of the excited electrons via phonon emission which finally leads to a non-equilibrium distribution of hot phonons. Indeed, although not explicitly mentioned in Ref. [Hag04], a loss of $\approx 90\,\%$ of the electronic energy within 0.5 ps after optical excitation has been found. Consequently, the decay of feature B in Fig. 5.12(c) with a 1-ps time constant must be due to the cooling of the hot phonons. This is considerably faster than in graphite where a 5.4-ps time constant was found and may point to a stronger ph-ph coupling in NTs.

5.9.4. Increased Absorption by Intraexcitonic Transitions?

As detailed above, feature B derives from rather delocalized electrons in the small-gap and metallic NTs. It is, however, rather unlikely that these tubes are also the origin of feature A, since this would imply the existence of electrons with 2 different localization lengths in the same tube type.

We propose the following explanation: Directly after excitation, the exciton population peaks sharply at the excitation energy in the E_{22}^{lg} band as shown in Fig. 5.16. This peak relaxes to the bottom of the E_{11}^{lg} band with a 40-fs time constant [Man05]. Note that
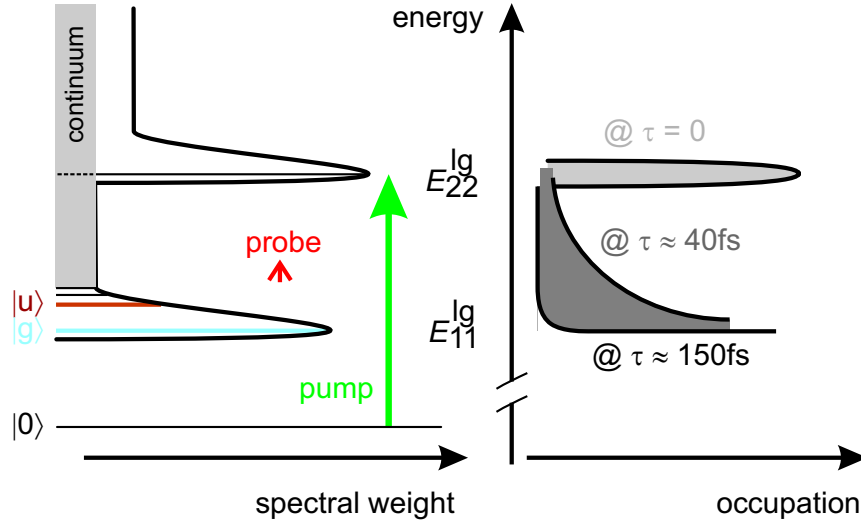
Figure 5.16.: Population relaxation of the excitonic levels. The pump pulse excites the E_{22}^{lg} exciton followed by a rapid redistribution of the exciton population with a 40-fs time constant [Man05]. Note that the excitonic energy has to be conserved in this process. Feature A is assigned to transitions between higher-lying excitonic levels with small excitation energy. The excitonic excess energy and, therefore, feature A decay with a 150-fs time constant due to heat transfer from the excited excitons to the optical phonons until the exciton is in its ground state. The THz photon energy amounts to about half of the transition energy between the g and u levels.

levels of higher energy cannot be completely depopulated in order to conserve the total energy [Rub05]. Feature A now arises from transitions between these higher-lying exciton states since their energetic spacing is comparable to the probe photon energy. The fast decay of A with a 150-fs time constant is due to energy transfer to the strongly coupled optical phonons which depopulates the higher-lying excitonic levels. Finally, only the E_{11}^{lg} ground state $|g\rangle$ is populated. Note that the next-higher state $|u\rangle$ has a by 0.2 eV higher energy [Wan05] and is thus not accessible by the THz probe pulse with photon energies of less than 0.15 eV.

The smaller localization length of the A excitations is assigned to the less effective screening of defects in the large-gap NTs than in the small-gap NTs which are the origin of feature B.

5.10. Conclusion and Outlook

In conclusion, time-resolved THz spectroscopy has been used to study single-wall carbon nanotubes. First, our data lack a distinct free-carrier response which is ascribed to the instantaneous generation of strongly bound excitons instead of free charge carriers as seen in graphite. Second, the transient dichroism directly displays the existence of charges that are spatially delocalized and localized with respect to a length scale of ~ 100 nm. The more delocalized excitations are attributed to carriers in the small-gap and metallic tubes

whereas the more localized excitations may arise from transitions between continuum states of excited excitons which decay with a 150-fs time constant.

The fact that all types of nanotubes compose our sample complicates the assignment of the features in the THz spectra. Meanwhile, the preparation of samples containing only large-gap tubes is possible [Rub05]. By investigating such a sample, the origin of the absorption feature A could be clarified. Alternatively, one can pump the present sample with THz radiation in order to excite only small-gap and metallic tubes. The amplified laser system in principle allows for the generation of sufficiently intense THz-pump pulses. At present, this setup is used to study the THz response of NTs excited with more intense visible pump pulses.